The impact of processing conditions and post-deposition oxidation on the opto-electrical properties of hydrogenated amorphous and nano-crystalline Germanium films

Vrijer, Thierry de; Ravichandran, Ashwath ; Bouazzata, Bilal ; Smets, Arno H.M.

DOI
10.1016/j.jnoncrysol.2020.120507

Publication date
2021

Document Version
Final published version

Published in
Journal of Non-Crystalline Solids

Journal of Non-Crystalline Solids 553 (2021) 120507

Contents lists available at ScienceDirect

Journal of Non-Crystalline Solids

journal homepage: www.elsevier.com/locate/jnoncrysol

The impact of processing conditions and post-deposition oxidation on the opto-electrical properties of hydrogenated amorphous and nano-crystalline Germanium films

Thierry de Vrijer *, Ashwath Ravichandran, Bilal Bouazzata, Arno H.M. Smets

Photovoltaic Materials and Devices, TU Delft, Mekelweg 4, Delft 2628CD, The Netherlands

ARTICLE INFO

Keywords:
germanium
PECVD
a-Ge:H
nanocrystalline
oxidation
germanium oxide

ABSTRACT

Low-cost multijunction photovoltaic devices are the next step in the solar energy revolution. Adding a bottom junction with a low bandgap energy material through plasma enhanced chemical vapor deposition (PECVD) processing could potentially provide a low-cost boost in conversion efficiency. A logical candidate for this low bandgap material is germanium. In this work we investigate the growth of PECVD processed hydrogenated amorphous/nano-crystalline germanium (a/nc-Ge:H), by characterizing over 100 samples, processed with a wide range of deposition pressures, powers, temperatures and GeH_4 dilution in hydrogen, using elemental analysis, vibrational analysis and analysis of the opto-electrical properties. We have identified a small processing window in which nc-Ge:H films are processed reproducibly. We also report on the strong correlation between the refractive index of the films and the presence- and extent of post-deposition oxidation. Notably, the oxidation generally increased the photoresponse of the films, as it results in a decrease of room temperature σ_d by 1-3 orders of magnitude. However, oxidation results in an increase of the bandgap energy and therefore impedes the development of a low bandgap material. The lowest E_{04} we report is about 1.1eV, with an E_{Tauc} of 0.9eV and an σ_{ph}/σ_d of 3.4.

1. Introduction

In 2015, for the first time in the history of photovoltaics, the PV module cost was no longer the dominant factor in the cumulative costs of installing a PV system [1]. This makes it even more crucial to increase the efficiency of PV devices, while maintaining low production costs. To that end a lot of effort is being devoted to develop a high bandgap absorber, often to partner with a crystalline silicon (c-Si) solar cell, the industry's workhorse. Examples of these are perovskite/c-Si tandems [2], GaAsP/c-Si tandems [3] and CZTS/c-Si tandems [4]. What these approaches have in common is that photons with an energy below 1.1eV are not utilized. A path to yet higher conversion efficiencies would be the utilization of these low energy photons. For the AM1.5G solar spectrum, a total of about $9.92ø10^{20} s^{-1}.m^{-2}$ photons are available in the 0.7eV-1.1eV spectral range, which equals a current density of 15.9 $mAøcm^{-2}$. For the 0.5-1.1eV spectral range the available current density is equal to 17.1 $mAøcm^{-2}$. A fraction of this current density would be large enough to not limit the output current of monolithically integrated 2-terminal multijunction devices such as an amorphous silicon/ nano-crystalline silicon/ crystalline silicon hybrid device [5], thin film silicon triple and quadruple junction devices [6–9] and the commercially available micromorph modules by [10] and [11]. All these devices are processed using plasma enhanced chemical vapor deposition (PECVD). Consequently, adding a bottom junction with a low bandgap energy material through PECVD processing, could potentially provide a low-cost boost in conversion efficiency.

A logical candidate for a PECVD processed low bandgap material is the group IV element germanium. Being larger and heavier than silicon, with its valence shell further removed from the nucleus, germanium forms weaker covalent bonds, resulting in a lower bandgap energy. In the past, attention has been devoted to processing hydrogenated amorphous germanium (a-Ge:H) through RF [12] and DC magnetron sputtering [13,14] thermal evaporation [15], and glow discharge chemical vapor deposition [16–25]. Limited work has been performed however on RF PECVD processing of thin film germanium [26,27]. In this work we investigate the growth of hydrogenated amorphous germanium and nanocrystalline germanium (nc-Ge:H), by performing a full characterization of the parameter space of processing conditions. To that end, well over 100 a/nc-Ge:H films are processed to characterize the influence of deposition temperature, power, pressure and GeH_4 dilution

* Corresponding author.

https://doi.org/10.1016/j.jnoncrysol.2020.120507
Received 28 July 2020; Received in revised form 19 October 2020; Accepted 20 October 2020
Available online 4 November 2020

in hydrogen, using elemental analysis, vibrational analysis and analysis of the opto-electrical properties.

2. Experimental section

Here, all reported films have a thickness of about 80-120nm. The films are simultaneously processed on 4 inch, 500μm thick mono-crystalline silicon wafers cut in quarters for Fourier Transform Infrared (FTIR) spectroscopy measurements, on 2cm x 1cm quartz substrates for Photothermal Deflection Spectroscopy (PDS) measurements and on 10cm x 2.5cm Corning Eagle XG glass for all other measurements. The films were processed in the Cascade RF-PECVD reactor, which has a circular electrode with a diameter of 160mm and an electrode spacing of 20mm. Cascade is a laminar flow reactor, where germane (GeH_4) and molecular hydrogen are used as precursor gasses.

FTIR spectra were obtained using a Thermo Fisher Nicolet 5700 spectrometer. The FTIR spectra were fitted using the Fityk freeware [28]. The background was subtracted manually. Fig. 1. Shows an example of a fitted FTIR spectrum. From the fitted spectra two material characteristics were determined. To facilitate extraction of these characteristics the absorbance spectrum was obtained from the transmission data using:

$$A_{abs}(\lambda) = \alpha(\lambda)d = \frac{T(\lambda)}{I_0(\lambda)} \tag{1}$$

Where A_{abs} is the absorbance, α is the material specific absorption coefficient, d is the thickness, T is the transmittance, and I_0 is the incident intensity. This simplification ignores the exponential decay of light through an absorptive medium. We argue this to be a valid assumption since $\alpha d < 0.01$.

The hydrogen concentration (C_H) was determined using the area of the Ge-H absorbance peak at 560cm^{-1}, using the following equation:

$$C_H = \frac{\rho_{Ge}}{\rho_H}\cdot\left(A\cdot\frac{A_{abs}(\omega)}{d}ln(10)\cdot\omega^{-1}\right) \tag{2}$$

where the part between brackets represents the hydrogen content N_H. C_H is calculated from N_H, through division of the hydrogen content by the atomic density of Hydrogen ρ_H over that of germanium ρ_{Ge}. Here ω is the wavenumber, d the thickness of the films, A_{abs} the area of the Gaussian measured around 560cm^{-1}. A is a proportionally constant which is amongst other things a function of the dipole mass, frequency and effective charge [29]. In this work, a value of $1.3\cdot10^{19}$cm^{-1}is used for A, which was determined by [30] and is in the same order as the value of $1.1\cdot10^{19}$cm^{-1}used by [31].

To quantitatively express the GeO_X peak intensity, as measured by FTIR, the absorption coefficient of the GeO_X peaks is used. This is done because multiple Gaussians are fitted in the 800-1050cm^{-1} range, with peak centres at roughly 846cm^{-1}, 860cm^{-1}, 930cm^{-1} and 1000cm^{-1}, likely corresponding to different GeO_X bonding configurations. These different bonding configurations make determining a single proportionally constant rather arbitrary. Therefore, the absorption coefficient of the summed GeO_X peaks (α_{GeO_X}) is used in this work as a thickness independent metric for sum of the relative GeO_X peak intensities. This metric is calculated by:

$$\alpha_{GeO_X} = d^{-1}\cdot ln(10)\cdot\sum\left(A_{absGeO_X}(\omega)\cdot\omega^{-1}\right) \tag{3}$$

It should also be noted that the GeO_X peaks in our samples are often, but not always, accompanied by absorbance peaks with a centre wavenumber of around 760cm^{-1} and 830cm^{-1}. These unidentified peaks are designated Ge_X in Fig. 1. The peak at 1100cm^{-1} is related to SiO_X bonds present on the surface of the silicon substrates.

The thickness, real part of the refractive index and optical bandgap energies were determined through Spectroscopic Ellipsometry (SE). The SE measurements were fitted using a Cody-Lorentz model. The E_{04} was determined by calculating the photon energy at which the absorption coefficient equals 10^4cm^{-1}. The E_{04} can therefore be considered an effective optical bandgap. The Tauc bandgap energy (E_{Tauc}) is reported at certain points in this work. The E_{Tauc} is closer to the electrical bandgap of the material and is obtained directly from the fitted model. The spectral absorption coefficient, as obtained from Photothermal Deflection Spectroscopy, of a few selected Ge:H films is shown in Fig. 2, so that the position of E_{04} with respect to the absorption curves can be determined.

Raman measurements were performed using a Renishaw inVia Raman Microscope, using an Argon laser with an operational wavelength of 514.5nm. The spectra are then fitted using Gaussian distributions at Raman shifts of 177 cm^{-1}, 230 cm^{-1} and 278 cm^{-1} for the LA, LO and TO amorphous germanium stretching modes [32,33] and an additional Gaussian distribution for the crystalline germanium peak at 300cm^{-1} [34,35]. No Gaussian was added for the a-Ge TA mode, as its Raman shift of about 80cm^{-1} is located outside of the measured range. The crystallinity (X_C) in this work is defined as:

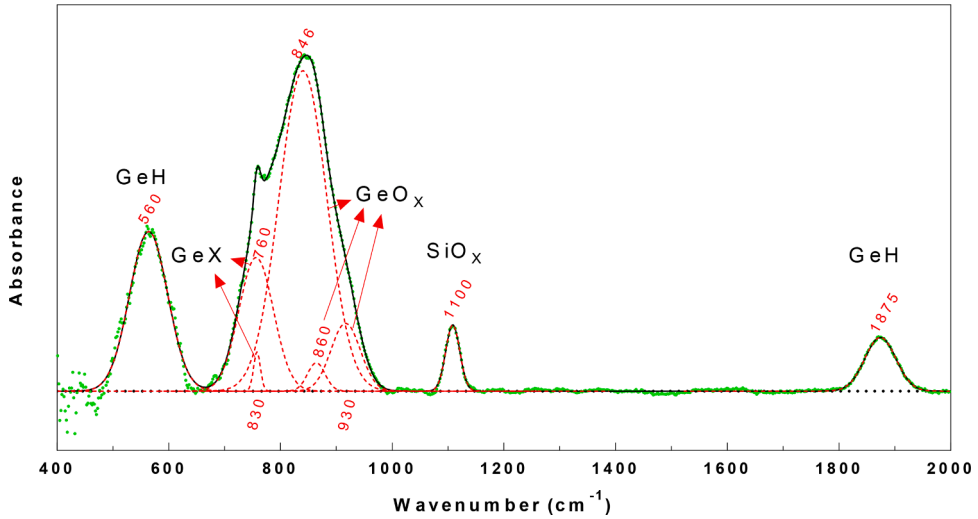

Fig. 1. Example of the fitted FTIR absorbance spectrum of a typical Ge:H film after oxidation. Green symbols indicate measured data after background correction. Black solid curve indicates fitted spectrum. Red curves indicate the individual fitted Gaussians. The centre wavenumbers of fitted Gaussians are indicated in red below/above the curves. The authors' identification of the fitted peaks are indicated in black above the fitted curves.

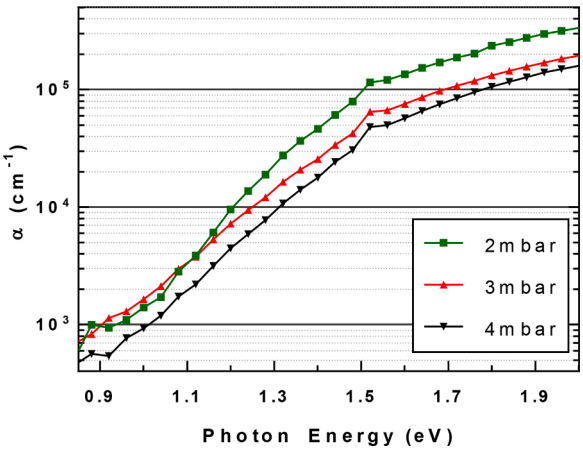

Fig. 2. Absorption coefficient as a function of photon energy for a few selected a-Ge:H films. Spectra are obtained from Photothermal Deflection Spectroscopy measurements. The films are processed at different pressures and at a $F(H_2)/F(GeH_4)$ of 400, 20W and 200°C.

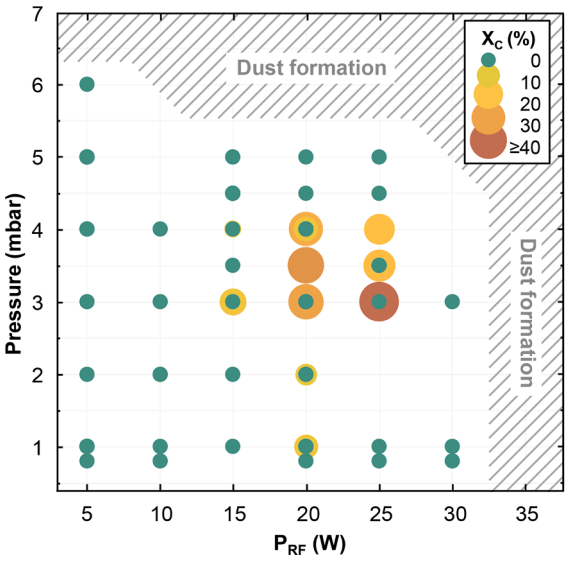

Fig. 3. Pressure plotted as a function of Power, for all processed Ge:H films. Crystallinity of films indicated by both the icon size and color. The shaded area indicates the boundaries of the processing window, where dust formation occurred.

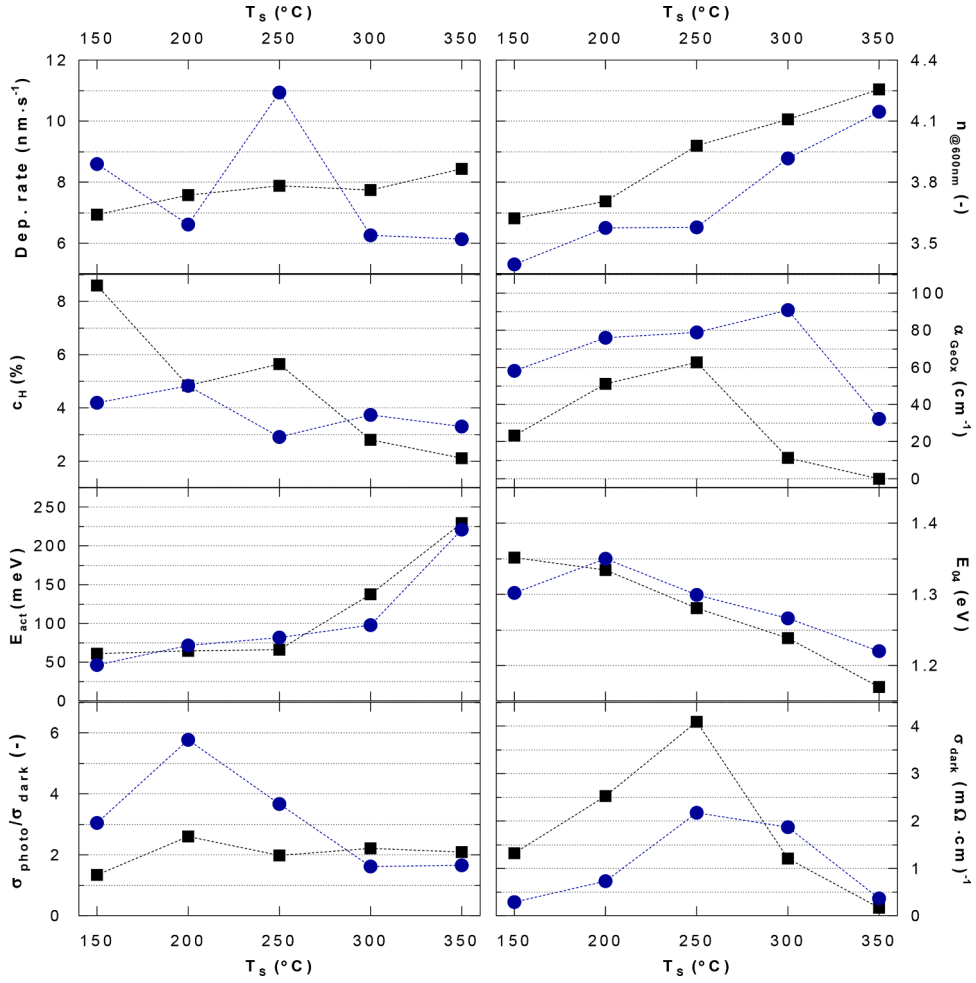

Fig. 4. The effect of substrate temperature on material properties. The samples represented by the blue circles are processed at 3.5mbar, 25W and a $F(H_2)/F(GeH_4)$ of 400. The dep.rate at 250°C for these samples has been omitted due to an error in recording the deposition time. Samples represented by black squares processed at 4.5mbar, 15W and a $F(H_2)/F(GeH_4)$ of 350.

$$X_C = \frac{I_{c-Ge}}{I_{c-Ge} + \gamma \cdot I_{a-Ge}} \quad (4)$$

Where I_{c-Ge} is the integrated area of the Gaussian corresponding to crystalline germanium and I_{a-Ge} is the area of the Gaussian of the a-Ge TO mode, the largest of a-Ge stretching modes. γ is a correction factor for the difference in cross section for phonon excitation of c-Ge with respect to a-Ge. In this work a value of 0.85 is used.

For the dark- and photo-conductivity measurements parallel electrodes consisting of 500nm-thick aluminum bars were evaporated onto the films. The dark conductivity at room temperature (σ_d), was determined by measuring the current at a fixed voltage of 10V for at different temperatures, ranging from 130°C to 60°C in 5°C increments, in a dark environment. From this measurement the activation energy (E_{act}) and pre-exponential factor σ_0 of the films was also calculated, using the Arrhenius equation:

$$\sigma_d = \sigma_0 \exp\left(\frac{-E_{act}}{k_b T}\right) \quad (5)$$

The photoconductivity (σ_{ph}) was calculated by measuring the current at a fixed voltage of 10V, using an AM1.5G solar simulator at an illumination of 100mWøcm^{-2}and a controlled temperature of 25°C. Finally, the setup used to obtain the PDS measurements is described in detail elsewhere [36].

3. Results and Discussion

3.1. The processing window

In this work we explore the full processing window for Ge:H thin films in our reactor, for a fixed electrode gap. The extent of this processing window is indicated in Fig. 3, where the crystallinity of the grown films is plotted as a function of the deposition pressure and power. The plotted powers and pressures represent the extent of the processing window, at a 20mm electrode gap. Dust formation occurred for samples processed at pressure above 5-6mbar and powers above 25-30W, as indicated in Fig. 3. For conditions below 5W and 0.5-0.8mbar a stable plasma could no longer be ignited. In Fig. 3 all processed samples are plotted. The size and colors of the symbols indicate the development of a crystalline germanium phase. A crystalline phase was only observed for certain samples processed at 200°C and at the highest $F(H_2)/F(GeH_4)$ of 400.

At power conditions of 20 W and 25 W and with increasing pressures, the material phase of the Ge:H films changes from amorphous to nanocrystalline at 2-3 mbar and from nanocrystalline back to amorphous at pressures above 4 mbar. This material phase dependence on pressure is qualitatively similar to what has been observed for Si:H alloys processed with a diluted silane plasma [38]. Although power densities in Ref. [38] are higher (due to higher dissociation energies for silane molecules in reference to the germane molecules) the dominant growth mechanisms are the same. At lower pressures the ion bombardment energy is too high and ion induced atom bulk displacement [41] results in an amorphous lattice. At a critical pressure the number of ion-neutral collisions in the plasma sheath are sufficient to reduce the ion energy below the threshold of ion-bulk displacement. At higher pressures the secondary reaction with atomic hydrogen H in the plasma bulk reduces the total H flux to the growth surface leading to amorphous growth again.

3.2. The influence of deposition temperature

Having determined the processing window, we consider the effect of varying a single deposition parameter. We start with the effect of the

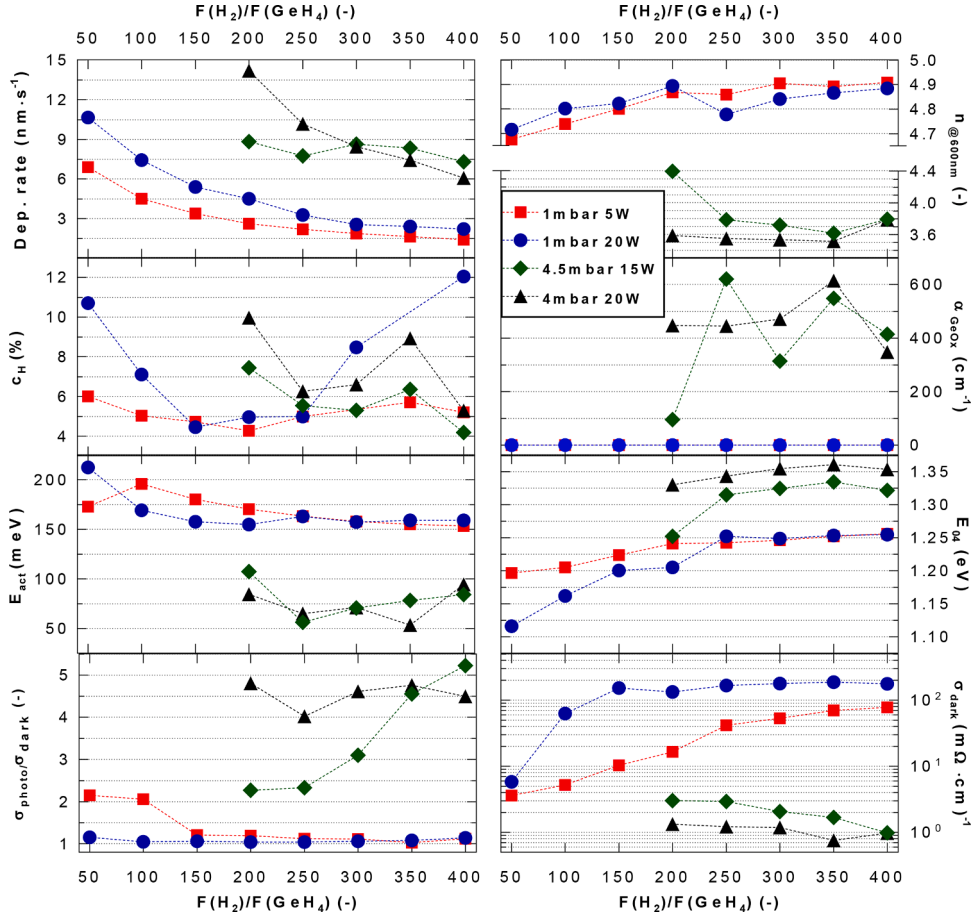

Fig. 5. Effect of hydrogen dilution on the measured material properties. The films are processed at 200°C. Deposition power and pressure are indicated in the legend.

substrate temperature (T_S) on the measured film characteristics, as presented in Fig. 4. In the case of silicon, processing conditions close to the amorphous-to-nanocrystalline transition regime produces the best quality amorphous material. For that reason, two sets of conditions are chosen that result in amorphous Ge:H films, but are close to the nc-Ge:H regime. The first characteristic that grabs the attention is the relatively high deposition rate, of several nanometers per second. This is 1-2 orders of magnitude higher than that of amorphous silicon in a similar PECVD reactor in our lab. The deposition rate slightly increases when T_S is increased, for the samples processed at 4.5mbar/15W. The samples processed at a lower pressure/power ratio do not show the same trend however. For both series, the refractive index ($n_{@600nm}$) steadily increases with temperature, while the hydrogen concentration (C_H) and the optical bandgap energy (E_{04}) steadily decrease. In fact, the E_{04} and $n_{@600nm}$ seem to linearly depend on the C_H, which is in line with earlier reports [18]. The E_{04},$n_{@600nm}$ and C_H trends indicate the growth of a less porous material with increasing T_S.

More information is provided by the presence of absorbance peaks in the FTIR spectra in the 850-1050cm^{-1} range. We suspect that the multiple peaks in this broad spectral range originate from GeO_X stretching modes, as a similar absorbance signature has been widely reported in oxygenated silicon samples [27,37–40]. With respect to the SiO_X stretching modes, the GeO_X peaks are shifted down by about 100-150cm^{-1}. This is in line with expectations since several Ge-H stretching modes are also shifted down with respect to their silicon counterparts. As to the origin of the GeO_X peaks, a large fraction Ge:H films do not have an GeO_X signature. It is therefore likely that the GeO_X bonds are formed during a post-deposition oxidation process. It should also be noted that the GeO_X peaks in our samples are often, but not always, accompanied by absorbance peaks with a centre frequency of around 760cm^{-1} and 830cm^{-1}. These peaks reportedly appear in environmentally unstable films hydrogenated germanium films [26]. The nature of these peaks is currently being investigated and will be published at a later time.

The absorption coefficient of the GeO_X peaks (α_{GeO_X}) has a maximum between a deposition temperature of 250°C and 300°C, which allows for the division into a low and high temperature region. In the lower temperature region, α_{GeO_X} steadily increases with deposition temperature. The underlying mechanism for this increase is not clear. In the high temperature region, the GeO_X peak intensity decreases. This is likely related to a reduction in the void density of the material, which reportedly occurs from a certain threshold temperature [21] and is in line with the increasing refractive index. We believe that the underlying cause of the decreasing void density is not the lack of dissociation of

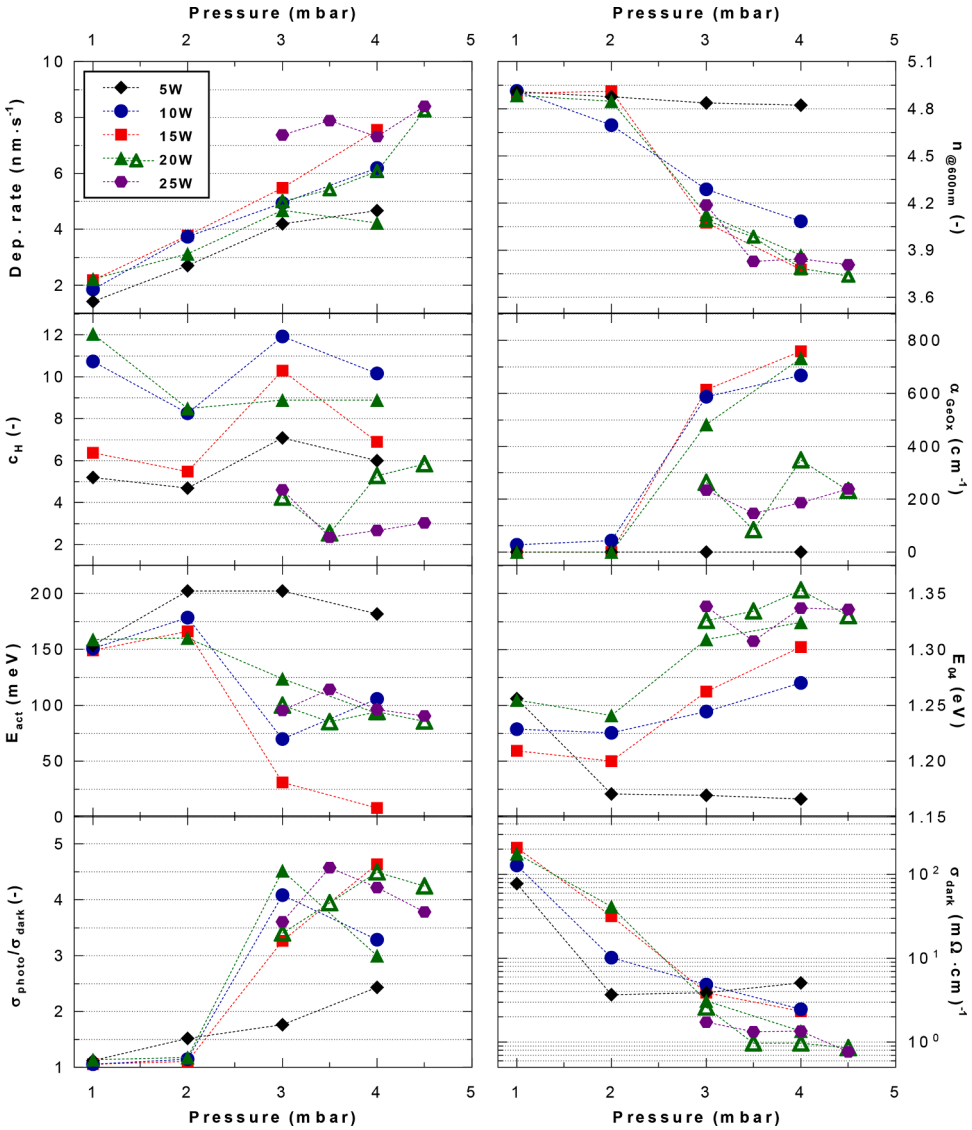

Fig. 6. Effect of deposition pressure and power on the material properties. The films are processed at 200°C and a $F(H_2)/F(GeH_4)$of 400.

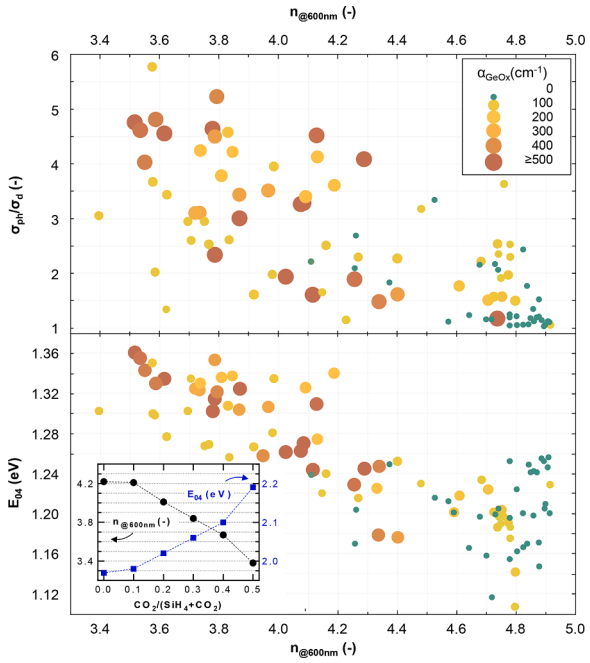

Fig. 7. σ_{ph}/σ_d (Top) and E_{04} (Bottom) plotted as a function of $n_{@600nm}$. α_{GeO_X} is indicated by the size and color of the icons. The small green symbols represent films for which no GeO_X signature was detected. Inset shows $n_{@600nm}$ (black circles) on the left y-axis and E_{04} (blue squares) on the right y-axis of intrinsic silicon oxide films as a function of the relative CO_2 flow rate ($CO_2/(SiH_4+CO_2)$)

larger Ge_2H_6 and Ge_3H_8 plasma phase polymers as described elsewhere [19]. Rather, the temperature dependence of void integration is surface diffusion controlled, as has been observed in amorphous silicon [29,41]. With respect to silicon, germanium is a relatively large and heavy atom, forming weaker chemical bonds. Consequently, germane dissociates more readily than silane [16,23,42], leading to a relatively large flux of Ge-radicals to the growing surface. Moreover, the Ge-radicals have much higher reactivity, so lower mobility, on the growing surface [43]. The large growth flux in combination with low surface diffusion result in a porous material with a relatively large void density. For the Ge-radicals incident on the growing surface to reach and fill a site that would result in a void, a certain activation energy is required. It is likely that, from a certain threshold temperature, small voids are filled. This results in a dense film that is resistant to post-oxidation of the bulk. The surface mobility of Ge-radicals and densification of the Ge:H tissue is further increased with increasing temperature, resulting in the total absence of a GeO_X signature for the higher pressure/power sample at 350°C. The surface-diffusion-controlled void incorporation is a function of the growth flux [41], which explains the different position of the threshold temperature for the 2 series in Fig. 4.

α_{GeO_X} has a strong correlation with the electrical properties of the a-Ge:H films. The films with a strong GeO_X signature have a relatively low activation energy (E_{act}) of 50-75meV. It has been reported that oxygen contamination of Ge films creates defects with energy levels close to the conduction band [13,46]. We have confirmed with Hall measurements that the samples are indeed n-type. In the high temperature regime, where α_{GeO_X} is strongly reduced, E_{act} increases to about 250meV. This value is still significantly less than half the bandgap energy, with a Tauc bandgap energy (E_{Tauc}) of around 1eV. In fact, none of the samples processed in this work, a large fraction of which had no FTIR peaks other than those related to Ge-H stretching, had an activation energy of over 280meV. This shows that the dominant defect type present in the amorphous germanium films have energy levels relatively close to the conduction band edge, which corroborates the conclusion of earlier work on glow-discharge a-Ge:H films [22]. The dark conductivity (σ_d) evolution as a function of T_S shows a strong correlation with the α_{GeO_X} trend. σ_d is highest for the samples with the strongest oxygen contamination. The dark conductivity for all these samples is relatively high, resulting in relatively poor photo/dark conductivity ratios (σ_{ph}/σ_d) of no more than 5-6. This relatively poor photoresponse of a/nc-Ge:H tissue, with respect to a/nc-Si:H, is in line with earlier reports [44,45].

In order to process device quality films, an effort should be made to decrease the deposition rate of the Ge:H films. This could potentially be achieved by changing I. the power and pressure at which the samples are processed, or II. by changing the dilution of the GeH_4 precursor in H_2. We start with an investigation of the latter.

3.3. The influence of GeH_4 dilution in H_2

Plotted in Fig. 5 are 2 curves processed at relatively low pressure and 2 curves processed at relatively high pressure. None of the samples processed in this series had a significant crystalline fraction. The deposition rate for all samples decreases with increasing $F(H_2)/F(GeH_4)$. This could be a result of increased atomic hydrogen etching with respect to the Ge growth flux. Alternatively, it could be a result of decreased availability of Ge-radicals in the plasma, or a combination of both. A slight deviation from the trends visible in some of the plots between a $F(H_2)/F(GeH_4)$ of 200 and 250 is likely a result of a change in absolute flow rate around that point, as H_2/GeH_4 is changed from 200sccm/1sccm to 125sccm/0.5sccm. For the low pressure samples, when $F(H_2)/F(GeH_4)$ is increased from 50 to about 200-250 the C_H and E_{act} decrease, while E_{04},$n_{@600nm}$ and σ_d increase. α_{GeO_X} shows that none of the low-pressure samples are oxygen contaminated. As to the underlying mechanism, apparently the complex environment created by increased atomic hydrogen etching, reduced availability of Ge-radicals and less energetic ion bombardment creates conditions in which the void

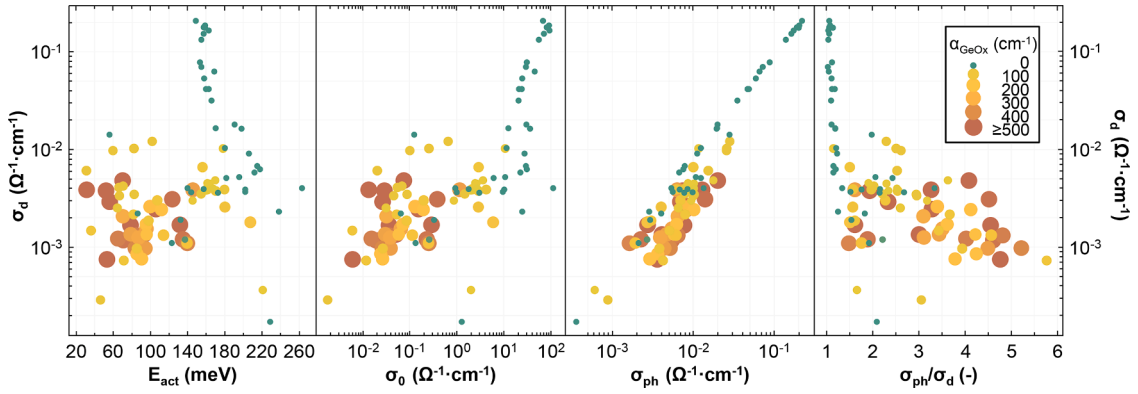

Fig. 8. The E_{act} (left, semi-log plot), σ_0 (centre left, log-log plot), σ_{ph} (centre right, log-log plot) and σ_{ph}/σ_d (right, semi-log plot) plotted as a function of σ_d. α_{GeO_X} is indicated by the size and color of the icons. The small green symbols represent films for which no GeO_X signature was detected

fraction decreases, making the material less porous. Moreover, in this environment C_H decreases, resulting in a decreased passivation fraction of Ge dangling bonds, thereby increasing the defect density in the material. As Ge defect states have energy levels closer to the conduction band [22], the material becomes slightly more n-type, resulting in a lower E_{act} and higher σ_d. The increased defect density also increases E_{04}, as defect related sub-bandgap absorption is increased. The high pressure samples largely show the same trends. However, the higher pressure results in more porous films, with lower $n_{@600nm}$ and a significant GeO_X signature. The presence of oxygen results in a lower E_{act}, higher E_{04}, and higher σ_{ph}/σ_d. Surprisingly, the presence of oxygen results in much lower σ_d, despite the much lower E_{act} of these samples. We'll discuss this in more detail later.

3.4. The influence of deposition pressure and power

In Fig. 6 the same material characteristics are plotted, for a range of powers, as a function of pressure. For all reported powers, the deposition rate increases as a function of pressure. This results in more porous material growth, as indicated by a decrease of $n_{@600nm}$. It should be noted that the $n_{@600nm}$ of the samples processed at 5W and 10W decrease linearly with increasing pressure, while the $n_{@600nm}$ drops significantly between 2 and 3 mbar. This is because the samples processed at $\leq$ 15W start to develop a crystalline phase, as shown in Fig. 3. The crystallinity of the Ge films influence the opto-electrical properties to a certain degree. The maximal σ_{ph}/σ_d, for instance, roughly coincide with the highest crystallinity fractions. However, the material properties are more strongly affected by the degree of oxidation. The σ_d,E_{04} and E_{act} all follow the α_{GeO_X} trend. Notably, E_{04} initially decreases between 1-2 mbar, when α_{GeO_X} is minimal, following the linear relation between $n_{@600nm}$,C_H and E_{04} as was observed in the temperature series.

3.5. The effect of post-deposition oxidation

The results from the previous sections seem to indicate that there is a strong correlation between the α_{GeO_X} and the opto-electrical properties. To gain some more insight nito the nature of this effect the E_{04} and σ_{ph}/σ_d are plotted as a function of $n_{@600nm}$ in Fig. 7. The α_{GeO_X} is indicated through the color and size of the icons. From this visual it is clear that with increasing GeO_X signature, both the E_{04} and σ_{ph}/σ_d are increased. In fact, E_{04} values of over 1.25eV and σ_{ph}/σ_d ratios of over 3.4 are only reached for samples with a significant GeO_X signature.

This raises 3 questions: I. Why does oxidation occur for some samples but not others? II. Why does oxidation lead to the increase of the E_{04}? III. And why does oxidation lead to an increase of the σ_{ph}/σ_d?

To gain some more insight into the first two questions, we consider the strong correlation between the E_{04} and $n_{@600nm}$. If the refractive index of the films decreases, the E_{04} is generally higher. Moreover, as the $n_{@600nm}$ decreases, both the fraction of films with $\alpha_{GeO_X}>0$ and the absolute value of α_{GeO_X} increases. In other words, the films without GeO_X signature are the films with a high refractive index. This means that films with a high density do not undergo post-deposition oxidation. As to the underlying cause, there are two plausible explanations. First, a decrease of the refractive index indicates an increase of the porosity and consequently the void density in the material. It might be that the defects present at the void surfaces are energetically well aligned with the reaction potential for the reaction resulting in GeO_X formation. This would mean that with increasing void density, the number of potential reaction sites for the GeO_X formation would increase. Increased porosity would thereby consequently lead to an increased α_{GeO_X}. However, in this case you might expect to see a more continuous increase of α_{GeO_X} with decreasing $n_{@600nm}$ than presented in this work. The oxidation as a function of $n_{@600nm}$ is near discrete. The second explanation is therefore more likely. For this we consider that the species responsible for the oxidation cannot diffuse into the material bulk when the Ge:H is too dense. The average Ge-Ge bond length in a relatively dense amorphous germanium film is about 2.46 [47], while the diameter of an H_2O molecule is about 2.75 [48]. Therefore, in a relatively dense a-Ge:H film, water vapor from the ambient would not be able to penetrate. If enough Ge atoms are missing from the amorphous lattice, so with a high enough void fraction, water vapor would be able to diffuse into the porous lattice. The in-diffusion of water molecules into the porous bulk would result in the observed oxidation of the a-Ge:H bulk. Besides this microscopic sensitivity to water induced oxidation, a similar effect can occur in the case of macroscopic cracks in the grown films, which is especially likely to occur in films with a relatively high crystalline fraction.

It is hard to make an assumption with respect to the causality of the relation between the level of oxidation and the $n_{@600nm}$. It is likely that more porous films will oxidize more strongly during the limited exposure time. On the other hand, increasing the level of oxidation of an amorphous material also generally results in a lower refractive index. An experiment with intrinsic amorphous silicon oxide, for instance, showed a strong decrease of the $n_{@600nm}$ with increasing CO_2 precursor gas flow rate during PECVD deposition, as shown in the inset in Fig. 7. This effect, a decrease of $n_{@600nm}$ with increased oxidation, has been reported earlier, both for intrinsic a-SiO_X:H [49] and a-GeO_X:H [13]. The fact that $n_{@600nm}$ does not scale linearly with α_{GeO_X} suggests that it might be a combination of both porosity facilitated oxidation and oxidation induced porosification.

To answer the third question, related to the origin of the σ_{ph}/σ_d increase with α_{GeO_X}, the E_{act}, pre-exponential factor (σ_0), σ_{ph} and σ_{ph}/σ_d are plotted as a function σ_d in Fig. 8, on semi-log and log-log axes. The σ_d,σ_0 and E_{act} are related according to Eq. 4. The E_{act} represents the difference between the Fermi level and the nearest band edge, which is the conduction band edge for a-Ge:H. Eq. 4 shows that there are two effects that influence σ_d. I. An increase of E_{act} decreases σ_d. II. an increase of σ_0 increases σ_d. The first effect is visible for the samples without GeO_X signature (green icons) with an E_{act} in the 150-250meV range (Fig. 8, left). For these samples, the σ_d clearly decreases with increasing E_{act}. The effect E_{act} has on the σ_d is minor however with respect to the increase of σ_0, that dominates the strong increase in σ_d. For the samples without GeO_X signature and σ_d above 10^{-2}, the increase in σ_{ph} is directly proportional to the increase in σ_d (Fig. 8, centre right), resulting in a constant σ_{ph}/σ_d of 1.

The largest σ_{ph}/σ_d are achieved for the samples with GeO_X signature. With respect to the samples without oxidation, they have an σ_d that is 1-3 orders of magnitude lower, despite much lower activation energies. The effect of the decreased σ_0 on the σ_d is much stronger than the σ_d

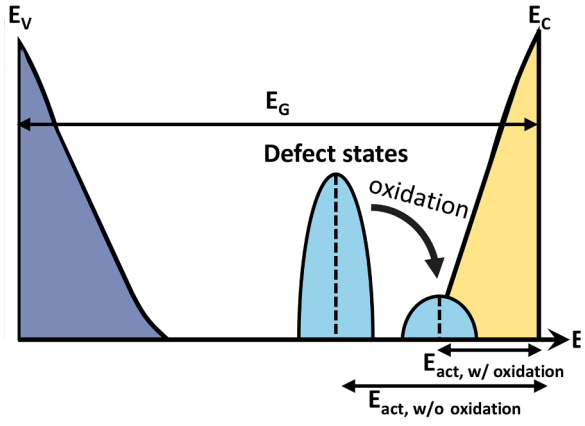

Fig. 9. Simplified density of states diagram showing the effect of oxidation on the Ge:H material. The blue area (left) and yellow area (right) represent the valence and conduction band tails, respectively. The light blue areas (centre) represent the defect states with and without oxidation. E_V is the valence band edge, E_C the conduction band edge, E_G the mobility gap of the Ge:H material.

increase resulting from the E_{act} decrease. Given that oxidation results in a decrease of σ_0 by 1-5 orders of magnitude, and the highest σ_{ph} are achieved by the un-oxidized samples, the improved σ_{ph}/σ_d ratios are clearly a result of a decreased σ_d rather than an increased σ_{ph}.

The question is why oxidation strongly decreases σ_0 in our Ge:H samples. Conductivity is a function of carrier density and mobility. The proportional increase of the σ_{ph} with the σ_d, in combination with the lack of additional photo-generated charge carriers upon external illumination, seems to indicate that high σ_d of the samples without GeO_X signature is the result of a high carrier density rather than high carrier mobility. The high carrier density is likely the result of a very high defect density. Upon oxidation both σ_0, indicative of the defect density, and E_{act}, indicative of the relative energy level of the dominant defect type (s), are decreased. The decrease of both metrics seems to suggest that the oxygen passivates the defects in a/nc-Ge:H, decreasing the defect density and consequently the σ_0 and σ_d. A simplified density of states diagram is presented in Fig. 9as a visual aid for the effect of oxidation on the defect density and average energy level. The formed GeO_X complexes have an energy level much closer to the conduction band, thereby shifting the Fermi level closer to the band edge and decreasing the E_{act}. In other words, a large density of defects with energy levels around 150-250meV from the conduction band edge is replaced by a much smaller defect density, closer the band edge.

4. Conclusion

In this work we investigate the influence of deposition temperature, power, pressure and the dilution of GeH_4 in H_2 on the material properties of well over a 100 PECVD processed a/nc-Ge:H films. We identified the processing window for Ge:H films in our reactor, with an electrode gap of 20mm. This window ranges from about 1-5mbar and 5-30W. nc-Ge:H films, with a crystallinity up to 54%, were obtained in the 15-25W range at 3-4mbar, 200°C, under the highest hydrogen dilution of $F(H_2)/F(GeH_4)$=400.

We found that there is a strong correlation between the refractive index and the presence of a GeO_X signature. We speculate that a high refractive index indicates a dense a-Ge:H network with a low void density, which prevents the in-diffusion of water from the ambient. This water vapour is responsible for the post-deposition oxidation of the Ge:H bulk. The oxidation has a very strong effect on the electrical properties of the films, as E_{act} is decreased, while σ_0 is strongly reduced. The decrease of σ_0 outweighs the increase of E_{act}, resulting in a decrease of σ_d by 1-3 orders of magnitude. We believe the oxygen has a passivating effect, decreasing the Ge-dangling bond related defect density in the bulk. The highest σ_{ph}/σ_d ratios of 5-6 are realized by Ge:H films with a GeO_X signature.

We've observed that the oxidation results in an increase of E_{04}. It therefore impedes the development of a low bandgap material. The lowest E_{04} we report is about 1.1eV, with an E_{Tauc} of 0.9eV and an σ_{ph}/σ_d of 3.4

CRediT authorship contribution statement

Thierry de Vrijer: Conceptualization, Supervision, Writing - original draft, Writing - review & editing. **Ashwath Ravichandran:** Investigation, Formal analysis. **Bilal Bouazzata:** Investigation, Formal analysis. **Arno H.M. Smets:** Conceptualization, Writing - review & editing, Funding acquisition.

Declaration of Competing Interest

The authors declare that they have no known competing financial interests or personal relationships that could have appeared to influence the work reported in this paper.

Acknowledgements

The authors would like to gratefully acknowledge the financial support from the Netherlands Organization for Scientific Research (NWO) Solar to Products grant and the support provided by Shell International Exploration & Production New Energies Research & Technology Dense Energy Carriers Program. We would also like to thank Martijn Tijssen for the support in preparing the reactor for Ge:H processing.

References

[1] S. Philipps, W. Warmuth, Photovoltaics report 2019, Tech. rep., Fraunhofer ISE (2019).
[2] M. Jaysankar, S. Paetel, E. Ahlswede, U.W. Paetzold, T. Aernouts, R. Gehlhaar, J. Poortmans, Toward scalable perovskitebased multijunction solar modules, Progress in Photovoltaics: Research and Applications (2019) 3153, https://doi.org/10.1002/pip.3153.
[3] S. Fan, Z.J. Yu, Y. Sun, W. Weigand, P. Dhingra, M. Kim, R.D. Hool, E.D. Ratta, Z. C. Holman, M.L. Lee, 20%-efficient epitaxial gaasp/si tandem solar cells, Solar Energy Materials and Solar Cells 202 (March) (2019) 110144, https://doi.org/10.1016/j.solmat.2019.110144.
[4] M. Valentini, C. Malerba, L. Serenelli, M. Izzi, E. Salza, M. Tucci, A. Mittiga, Fabrication of monolithic CZTS/si tandem cells by development of the intermediate connection, Solar Energy 190 (2019) 414–419, https://doi.org/10.1016/j.solener.2019.08.029.
[5] S. Kirner, H. Sarajan, A. Azarpira, T. Schedel-Niedrig, B. Stannowski, B. Rech, R. Schlatmann, Wafer surface tuning for a-si:h/μ c-si:h/c-si triple junction solar cells for application in water splitting, Energy Procedia 102 (2016) 126–135, https://doi.org/10.1016/j.egypro.2016.11.327.
[6] J.-W. Schüttauf, B. Niesen, L. Löfgren, M. Bonnet-Eymard, M. Stuckelberger, S. Hänni, M. Boccard, G. Bugnon, M. Despeisse, F.-J. Haug, F. Meillaud, C. Ballif, Amorphous silicongermanium for triple and quadruple junction thin-film silicon based solar cells, Solar Energy Materials and Solar Cells 133 (2015) 163–169, https://doi.org/10.1016/j.solmat.2014.11.006.
[7] D.Y. Kim, E. Guijt, F.T. Si, R. Santbergen, J. Holovský, O. Isabella, R.A. van Swaaij, M. Zeman, Fabrication of double- and triple-junction solar cells with hydrogenated amorphous silicon oxide (a-siox:h) top cell, Solar Energy Materials and Solar Cells 141 (2015) 148–153, https://doi.org/10.1016/j.solmat.2015.05.033.
[8] F.T. Si, O. Isabella, H. Tan, M. Zeman, Quadruple-junction thin-film silicon solar cells using four different absorber materials, Solar RRL 1 (3-4) (2017) 1700036, https://doi.org/10.1002/solr.201700036.
[9] Y. Cao, X. Zhu, X. Tong, J. Zhou, J. Ni, J. Zhang, J. Pang, Ultrathin microcrystalline hydrogenated si/ge alloyed tandem solar cells towards full solar spectrum conversion, Frontiers of Chemical Science and Engineering (2019), https://doi.org/10.1007/s11705-019-1906-0.
[10] J. Hoetzel, O. Caglar, J. Cashmore, C. Goury, J. Kalas, M. Klindworth, M. Kupich, G.-F. Leu, M.-H. Lindic, P. Losio, T. Mates, B. Mereu, T. Roschek, I. Sinicco, Microcrystalline bottom cells in large area thin film silicon MICROMORPH^{TM} solar modules, Solar Energy Materials and Solar Cells 157 (2016) 178–189, https://doi.org/10.1016/j.solmat.2016.05.043.
[11] K. Jäger, J. Lenssen, P. Veltman, E. Hamers, Large-area production of highly efficient flexible light-weight thin-film silicon PV modules. Proc. of the 28th European Photovoltaic Solar Energy Conference, 2013, pp. 2164–2169.
[12] J.R. Blanco, P.J. McMarr, J.E. Yehoda, K. Vedam, R. Messier, Density of amorphous germanium films by spectroscopic ellipsometry, Journal of Vacuum Science & Technology A: Vacuum, Surfaces, and Films 4 (3) (1986) 577–582, https://doi.org/10.1116/1.573851.
[13] B. Schröder, A. Annen, T. Drüsedau, H. Freistedt, P. Deák, H. Oechsner, Influence of oxygen incorporation on the properties of magnetron sputtered hydrogenated amorphous germanium films, Applied Physics Letters 62 (16) (1993) 1961–1963, https://doi.org/10.1063/1.109504.
[14] A. Scholz, B. Muller, B. Schroder, H. Oechsner, H. Freistedt, Photoconductivity spectroscopy (CPM) on a-ge:h at low temperatures, Journal of Non-Crystalline Solids 164-166 (1993) 375–378.
[15] V. Sorianello, L. Colace, G. Assanto, M. Nardone, Micro-raman characterization of germanium thin films evaporated on various substrates, Microelectronic Engineering 88 (4) (2011) 492–495, https://doi.org/10.1016/j.mee.2010.10.028.
[16] F.H. Karg, H. Bohm, K. Pierz, Influence of plasma deposition on structural and electronic properties of a-ge:h, Journal of Non-Crystalline Solids 114 (1989) 477–479.
[17] W.A. Turner, S.J. Jones, D. Pang, B.F. Bateman, J.H. Chen, Y. Li, F.C. Marques, A. E. Wetsel, P. Wickboldt, W. Paul, J. Bodart, R.E. Norberg, I.E. Zawawi, M.L. Theye, Structural, optical, and electrical characterization of improved amorphous hydrogenated germanium, Journal of Applied Physics 67 (12) (1990) 7430–7438, https://doi.org/10.1063/1.344533.
[18] T. Nakashita, A. Inoue, S. Hagiwara, F. Uehara, K. Kohno, Dependence of electronic properties of hydrogenated amorphous ge on deposition condition, Japanese Journal of Applied Physics 31 (1992) 1730–1736, https://doi.org/10.1143/JJAP.31.1730.Part 1, No. 6A
[19] G. Lucovsky, S.S. Chao, J. Yang, J.E. Tyler, R.C. Ross, W. Czubatyj, Chemical bonding of hydrogen and oxygen in glow-discharge-deposited thin films of a-ge:h

and a-ge:(h,o), Physical Review B 31 (4) (1985) 2190–2197, https://doi.org/10.1103/PhysRevB.31.2190.
[20] J.R. Doyle, D.A. Doughty, A. Gallagher, Germane discharge chemistry, Journal of Applied Physics 69 (8) (1991) 4169–4177, https://doi.org/10.1063/1.348384.
[21] K. Eberhardt, G. Bauer, Effect of h-content and h-bonding configuration on light and thermal induced metastability in amorphous hydrogenated germanium (a-ge:h), Journal of Non-Crystalline Solids 164-166 (PART 1) (1993) 19–22, https://doi.org/10.1016/0022-3093(93)90482-D.
[22] M. Stutzmann, J. Stuke, H. Dersch, Electron spin resonance of doped glow-discharge amorphous germanium, physica status solidi (b) 115 (1) (1983) 141–151, https://doi.org/10.1002/pssb.2221150116.
[23] J.R. Doyle, D.A. Doughty, A. Gallagher, Plasma chemistry in silane/germane and disilane/germane mixtures, Journal of Applied Physics 71 (10) (1992) 4727–4738, https://doi.org/10.1063/1.350663.
[24] K. Gruntz, L. Ley, M. Cardona, R. Johnson, G. Harbeke, B.v. Roedern, Photoemission spectroscopy of amorphous hydrogenated germanium, Journal of Non-Crystalline Solids 35 (36) (1980) 453–458.
[25] C. Li, J. Ni, X. Sun, X. Wang, Z. Li, H. Cai, J. Li, J. Zhang, Nanocrystalline germanium nip solar cells with spectral sensitivities extending into 1450 nm, Journal of Physics D 50 (4) (2017) 045108, https://doi.org/10.1088/1361-6463/aa4f93.
[26] W. Paul, Structural, optical and photoelectronic properties of improved PECVD a-ge:h, Journal of Non-Crystalline Solids 137 (138) (1991) 803–808.
[27] G. Lucovsky, R.J. Nemanich, J.C. Knights, Structural interpretation of the vibrational spectra of a-si: H alloys, Physical Review B 19 (4) (1979) 2064–2073, https://doi.org/10.1103/PhysRevB.19.2064.
[28] M. Wojdyr, Fityk : a general-purpose peak fitting program, Journal of Applied Crystallography 43 (5) (2010) 1126–1128, https://doi.org/10.1107/S0021889810030499.
[29] A.H.M. Smets, M.C.M. van de Sanden, Relation of the si-h stretching frequency to the nanostructural si-h bulk environment, Physical Review B 76 (7) (2007) 073202, https://doi.org/10.1103/PhysRevB.76.073202.
[30] M.S. Abo-Ghazala, S.A. Hazmy, Hydrogen bonding in hydrogenated amorphous germanium, Tsinghua Science and Technology 9 (2) (2004) 177–180.
[31] M. Cardona, Vibrational spectra of hydrogen in silicon and germanium, physica status solidi (b) 118 (2) (1983) 463–481, https://doi.org/10.1002/pssb.2221180202.
[32] D. Bermejo, M. Cardona, Raman scattering in pure and hydrogenated amorphous, Journal of Non-Crystalline Solids 32 (1978) 405–419.
[33] O. Madelung, U. Rossler, M. Schulz, Germanium (ge) raman phonon frequencies and wavenumbers. Group IV Elements, IV-IV and III-V Compounds. Part a - Lattice Properties volume 4, Springer-Verlag, Berlin/Heidelberg, 2001, pp. 1–17, https://doi.org/10.1007/10551045_228.
[34] V.A. Volodin, G.K. Krivyakin, G.D. Ivlev, S.L. Prokopyev, S.V. Gusakova, A. A. Popov, Crystallization of amorphous germanium films and multilayer a-ge/a-si structures upon exposure to nanosecond laser radiation, Semiconductors 53 (3) (2019) 400–405, https://doi.org/10.1134/S1063782619030217.
[35] P. Alfaro-Calderón, M. Cruz-Irisson, C. Wang-Chen, Theory of raman scattering by phonons in germanium nanostructures, Nanoscale Research Letters 3 (2) (2008) 55–59, https://doi.org/10.1007/s11671-007-9114-0.
[36] Z. Remes, R. Vasudevan, K. Jarolimek, A.H. Smets, M. Zeman, The optical spectra of a-si:h and a-sic:h thin films measured by the absolute photothermal deflection spectroscopy (PDS), Solid State Phenomena 213 (2014) 19–28.10.4028/www.scientific.net/SSP.213.19
[37] G. Talukder, J.C.L. Cornish, P. Jennings, G.T. Hefter, B.W. Clare, J. Livingstone, Effects of annealing on infrared and thermaleffusion spectra of sputtered a si:h alloys, Journal of Applied Physics 71 (1) (1992) 403–409, https://doi.org/10.1063/1.350723.
[38] A.H.M. Smets, T. Matsui, M. Kondo, High-rate deposition of microcrystalline silicon p-i-n solar cells in the high pressure depletion regime, Journal of Applied Physics 104 (3) (2008) 034508, https://doi.org/10.1063/1.2961334.
[39] A. Bronneberg, A. Smets, M. Creatore, M.v.de. Sanden, On the oxidation mechanism of microcrystalline silicon thin films studied by fourier transform infrared spectroscopy, Journal of Non-Crystalline Solids 357 (3) (2011) 884–887, https://doi.org/10.1016/j.jnoncrysol.2010.11.001.
[40] Y.-P. Chou, S.C. Lee, Structural, optical, and electrical properties of hydrogenated amorphous silicon germanium alloys, Journal of Applied Physics 83 (8) (1998) 4111–4123, https://doi.org/10.1063/1.367229.
[41] A.H.M. Smets, W.M.M. Kessels, M.C.M. van de Sanden, Surface-diffusion-controlled incorporation of nanosized voids during hydrogenated amorphous silicon film growth, Applied Physics Letters 86 (4) (2005) 041909, https://doi.org/10.1063/1.1853508.
[42] Y.H. Shing, J.W. Perry, C.E. Allevato, Amorphous silicon germanium alloy film deposition with in situ plasma diagnostics, Solar Cells 24 (1988) 353–362.
[43] A. Bhaduri, P. Chaudhuri, S. Vignoli, C. Longeaud, Correlation of structural inhomogeneities with transport properties in amorphous silicon germanium alloy thin films, Solar Energy Materials and Solar Cells 94 (9) (2010) 1492–1495, https://doi.org/10.1016/j.solmat.2010.02.043.
[44] Y. Cao, Y. Liu, J. Zhou, Y. Wang, J. Ni, J. Zhang, Non-uniform distribution in $\mu c - si_{1-x}Ge_X$:H and its influence on thin film and device performance, Solar Energy Materials and Solar Cells 151 (2016) 1–6, https://doi.org/10.1016/j.solmat.2016.02.009.
[45] T. Matsui, K. Ogata, C.W. Chang, M. Isomura, M. Kondo, Carrier collection characteristics of microcrystalline silicongermanium pin junction solar cells, Journal of Non-Crystalline Solids 354 (19-25) (2008) 2468–2471, https://doi.org/10.1016/j.jnoncrysol.2007.09.026.
[46] M. Moreno, N. Delgadillo, A. Torres, R. Ambrosio, P. Rosales, A. Kosarev, C. Reyes-Betanzo, J. de la Hidalga-Wade, C. Zuniga, W. Calleja, Boron doping compensation of hydrogenated amorphous and polymorphous germanium thin films for infrared detection applications, Thin Solid Films 548 (2013) 533–538, https://doi.org/10.1016/j.tsf.2013.08.102.
[47] T.A. Abtew, D.A. Drabold, Ab initio models of amorphous $si_{1-x}Ge_X$:H, Physical Review B 75 (4) (2007) 045201, https://doi.org/10.1103/PhysRevB.75.045201.
[48] R.L. Redington, D.E. Milligan, Infrared spectroscopic evidence for the rotation of the water molecule in solid argon, The Journal of Chemical Physics 37 (10) (1962) 2162–2166, https://doi.org/10.1063/1.1732982.
[49] D.Y. Kim, E. Guijt, R.A.C.M.M. van Swaaij, M. Zeman, Development of $a - SiO_X$:h solar cells with very high voc x FF product, Progress in Photovoltaics: Research and Applications 23 (6) (2015) 671–684, https://doi.org/10.1002/pip.2581.